

Banner appropriate to article type will appear here in typeset article

# Velocity gradient partitioning in turbulent flows

Rahul Arun<sup>1</sup>† and Tim Colonius<sup>2</sup>

<sup>1</sup>Graduate Aerospace Laboratories, California Institute of Technology, Pasadena, CA 91125, USA

<sup>2</sup>Department of Mechanical and Civil Engineering, California Institute of Technology, Pasadena, CA 91125, USA

(Received xx; revised xx; accepted xx)

The velocity gradient tensor can be decomposed into axial straining, pure shearing, and rigid rotation tensors, each with distinct symmetry and normality properties. We partition the strength of velocity gradient fluctuations based on the relative contributions of these constituents in several turbulent flows. These flows include forced isotropic turbulence, channels and boundary layers, and subsonic and transonic jets. For forced isotropic turbulence, the partitioning is in excellent agreement with previous results. For wall-bounded turbulence, the partitioning collapses onto the isotropic partitioning far from the wall, where the mean shearing is relatively weak. By contrast, the near-wall partitioning is dominated by shearing. Between these two regimes, the partitioning collapses well at sufficiently high friction Reynolds numbers and its variations in the buffer layer and the log-law region can be reasonably modeled as a function of the mean shearing strength. The isotropic partitioning also applies throughout much of the turbulent jets due to the rapid decay of the mean flow shear layer near the nozzle lip. Before reaching the exterior potential flow regime, the relative contribution of rigid rotation around the turbulent/non-turbulent interface is enhanced with respect to the isotropic partitioning. Altogether, our results highlight the broad applicability of the velocity gradient partitioning to turbulence modeling.

**Key words:** turbulence modeling, isotropic turbulence, turbulent boundary layers

## 1. Introduction

Velocity gradients describe fundamental statistical and structural features of small-scale turbulence (Meneveau 2011; Johnson & Wilczek 2024). Partitioning the velocity gradient tensor (VGT) based on its symmetry and normality properties distinguishes the contributions of three distinct modes of deformation to these features. These modes of deformation are axial straining (symmetric/normal), rigid rotation (antisymmetric/normal), and pure shearing (non-normal).

Kolář (2004, 2007) originally formulated this so-called “triple decomposition” of the VGT with the aim of identifying a “basic” reference frame in which the effects of pure shearing can be extracted. While identifying such a frame originally required solving challenging

† Email address for correspondence: [rarun@caltech.edu](mailto:rarun@caltech.edu)

pointwise optimization problems, more computationally practical approaches based on the real Schur decomposition of the VGT have been developed recently (Liu *et al.* 2018; Gao & Liu 2018, 2019). A complex Schur decomposition can also be used (Keylock 2018), although its relationship to basic reference frames in physical space is less clear (Kronborg & Hoffman 2023).

Partitioning the strength of the VGT based on its triple decomposition provides an expressive description of flow features. For example, the contribution of rigid rotation has found use in identifying vortices (Liu *et al.* 2018; Gao & Liu 2018; Arun & Colonius 2024) and the contribution of shearing has been shown to be pivotal in driving intermittency (Das & Girimaji 2020) and dissipation (Wu *et al.* 2020) in turbulent flows. The interplay between shearing and rigid rotation has also been used to characterize the transition and turbulent decay of colliding vortex rings mediated by the elliptic instability (Arun & Colonius 2024).

Das & Girimaji (2020) showed that the velocity gradients in forced isotropic turbulence converge to a specific partitioning at high Taylor-scale Reynolds numbers. More recently, Arun & Colonius (2024) found that the decaying turbulent cloud produced by a vortex ring collision follows a similar partitioning. However, the spatial development in flows such as wakes, axisymmetric jets, and mixing layers has been associated with enhanced contributions of non-normal (i.e., shearing) velocity gradients (Beumard *et al.* 2019). Beyond the strength of velocity gradients, the triple decomposition has also found use in analyzing nonlinear terms relevant to turbulence modeling, including the Reynolds stress tensor (Enoki *et al.* 2023) and vortex stretching and strain self-amplification (Keylock 2018).

Building on these previous works, we aim to broadly characterize the relevance of the triple decomposition of the VGT in turbulent flows. Specifically, we partition the strength of velocity gradient fluctuations in forced isotropic turbulence, channels and boundary layers, and subsonic and transonic jets. For the wall-bounded flows, we aim to characterize how the partitioning is affected by the mean shearing and the friction Reynolds number. For the jets, we also aim to characterize how the partitioning within the jet differs from that near the turbulent/non-turbulent (T/NT) interface. The partitioning framework is presented in §2 and the turbulence datasets we analyze are reported in §3. We establish the isotropic partitioning in §4 and thereafter discuss how the partitioning is modified in wall-bounded turbulence (§5) and in jets (§6).

## 2. Partitioning framework

We consider the VGT,  $\mathbf{A} = \nabla \mathbf{u}$ , associated with turbulent velocity fluctuations,  $\mathbf{u} = \mathbf{U} - \bar{\mathbf{u}}$ , where  $\mathbf{U}$  and  $\bar{\mathbf{u}}$  represent the total and mean velocities, respectively. The VGT can be expressed in its principal reference frame, denoted by  $(\cdot)^*$ , as  $\mathbf{A}^* = \mathbf{Q}\mathbf{A}\mathbf{Q}^T$ , where  $\mathbf{Q}$  is unitary and  $(\cdot)^T$  represents the transpose. In this frame, the VGT is quasi-triangular and its triple decomposition can be expressed as

$$\mathbf{A}^* = \underbrace{\begin{bmatrix} \dot{\epsilon}_1^* & 0 & 0 \\ 0 & \dot{\epsilon}_2^* & 0 \\ 0 & 0 & \dot{\epsilon}_3^* \end{bmatrix}}_{\mathbf{A}_\epsilon^*} + \underbrace{\begin{bmatrix} 0 & 0 & 0 \\ 0 & 0 & \dot{\varphi}_1^* \\ 0 & -\dot{\varphi}_1^* & 0 \end{bmatrix}}_{\mathbf{A}_\varphi^*} + \underbrace{\begin{bmatrix} 0 & \dot{\gamma}_3^* & \dot{\gamma}_2^* \\ 0 & 0 & \dot{\gamma}_1^* \\ 0 & 0 & 0 \end{bmatrix}}_{\mathbf{A}_\gamma^*}, \quad (2.1)$$

where  $\mathbf{A}_\epsilon^*$ ,  $\mathbf{A}_\varphi^*$ , and  $\mathbf{A}_\gamma^*$  represent the axial straining, rigid rotation, and pure shearing tensors, respectively. These tensors can be determined and transformed to the original coordinate system using the ordered real Schur decomposition of  $\mathbf{A}$  (Kronborg & Hoffman 2023).

Correspondingly, the strength of the turbulent velocity gradients can be expressed as

$$A^2 = \text{tr}(\mathbf{A}^T \mathbf{A}) = \underbrace{\text{tr}(\mathbf{A}_\epsilon^T \mathbf{A}_\epsilon)}_{A_\epsilon^2} + \underbrace{\text{tr}(\mathbf{A}_\varphi^T \mathbf{A}_\varphi)}_{A_\varphi^2} + \underbrace{\text{tr}(\mathbf{A}_\gamma^T \mathbf{A}_\gamma)}_{A_\gamma^2} + 2\underbrace{\text{tr}(\mathbf{A}_\varphi^T \mathbf{A}_\gamma)}_{A_{\varphi\gamma}^2}, \quad (2.2)$$

where  $\text{tr}(\cdot)$  represents the trace. The first three terms represent the strengths of the constituents in (2.1) and the last term represents the interaction between shearing and rigid rotation. The velocity gradient partitioning is defined in terms of the relative contributions of these constituents to  $A^2$ . In normalized form, these contributions are bounded as  $A_\epsilon^2/A^2 \in [0, 1]$ ,  $A_\varphi^2/A^2 \in [0, 1]$ ,  $A_\gamma^2/A^2 \in [0, 1]$ , and  $A_{\varphi\gamma}^2/A^2 \in [0, (\sqrt{2} + 1)^{-1}]$  (Das & Girimaji 2020).

Ensemble averaging can be used to characterize the statistical relevance of the contributions in this partitioning. We define the averaged partitioning as

$$\langle A_\zeta^2 \rangle_{A^2} = \langle A_\zeta^2 \rangle / \langle A^2 \rangle, \quad \zeta \in \{\epsilon, \varphi, \gamma, \varphi\gamma\}, \quad (2.3)$$

where  $\langle \cdot \rangle$  denotes averaging over homogeneous spatial directions and time. The present study focuses on this averaged partitioning, which characterizes contributions to enstrophy and dissipation (Das & Girimaji 2020; Arun & Colonius 2024).

### 3. Turbulence datasets

As summarized in table 1, we analyze the partitioning in several well-validated turbulence datasets. These datasets include forced isotropic turbulence (FIT315 and FIT610), wall-bounded turbulence (Ch0186, Ch1000, BL0729, BL1024), and jet turbulence (Jet0.4 and Jet0.9) over a broad range of Reynolds numbers. The isotropic and wall-bounded datasets represent direct numerical simulations and the jet datasets represent large-eddy simulations near practical operating conditions (Brès *et al.* 2018). FIT610 and Ch1000 are obtained from the Johns Hopkins Turbulence Databases (Li *et al.* 2008) and Ch0186 represents a minimal flow unit for near-wall turbulence (Jiménez & Moin 1991). The references in table 1 provide further computational details and validation for each dataset.

We establish the isotropic partitioning using FIT610 and test its sensitivity to  $Re_\lambda$  using FIT315. The snapshots for FIT315 are spaced roughly one integral time unit apart and  $N_t$  is selected to produce a similar number of samples to FIT610. We use Ch1000 to characterize the partitioning in a turbulent channel at a moderate  $Re_\tau$ . Its snapshots are spaced roughly 0.65 eddy turnover time units apart and they span roughly one flow-through time unit (Graham *et al.* 2016). Ch0186 allows us to investigate how the wall-bounded partitioning changes when  $Re_\tau$  is barely large enough to sustain turbulence. Its snapshots span roughly 160 eddy turnover time units. We use BL0729 and BL1024 to further characterize the partitioning for wall-bounded turbulence subject to mild spatial development. Their broad ranges of  $Re_\tau$  allow us to characterize how the partitioning evolves as the flows become increasingly turbulent. The snapshots for BL0729 and BL1024 span more than 20 and 7 eddy turnover time units, respectively (Towne *et al.* 2023).

When computing the VGT, we adopt the differentiation techniques employed in the original simulations where possible. We further require that all elements of the VGT be collocated prior to partitioning. For FIT315 and FIT610, we use a spectral method to compute all velocity gradients. For Ch0186, we use the second-order accurate staggered finite differences employed in the original simulation and subsequently shift staggered quantities to cell centers. This shifting is performed by adjusting the phases of the Fourier modes in  $x$  and  $z$  and by averaging adjacent values in  $y$  (Arun *et al.* 2023). For Ch1000, we use a spectral method in  $x$  and  $z$  and collocated finite differences with a stencil size of  $N_s = 7$  in  $y$ . The

---

Case	Configuration	Reynolds number	Grid size	$N_t$	Reference
FIT315	Forced isotropic	$Re_\lambda \approx 315$	(1024, 1024, 1024)	67	Cardesa <i>et al.</i> (2017)
FIT610	Forced isotropic	$Re_\lambda \approx 610$	(4096, 4096, 4096)	1	Yeung <i>et al.</i> (2012)
Ch0186	Channel	$Re_\tau \approx 186$	( 32, 129, 32)	55 925	Arun <i>et al.</i> (2023)
Ch1000	Channel	$Re_\tau \approx 1000$	(2048, 512, 1536)	40	Graham <i>et al.</i> (2016)
BL0729	Boundary layer	$Re_\tau \approx 292 - 729$	(2049, 90, 256)	10 000	Towne <i>et al.</i> (2023)
BL1024	Boundary layer	$Re_\tau \approx 481 - 1024$	(4097, 90, 512)	1500	Towne <i>et al.</i> (2023)
Jet0.4	Subsonic jet	$Re_j \approx 450\,000$	( 656, 138, 128)	10 000	Heidt <i>et al.</i> (2023)
Jet0.9	Transonic jet	$Re_j \approx 1\,018\,400$	( 656, 138, 128)	10 000	Towne <i>et al.</i> (2023)

---

Table 1: Turbulence datasets considered in the present analyses. Taylor-scale, friction, and jet Reynolds numbers are denoted by  $Re_\lambda$ ,  $Re_\tau$ , and  $Re_j$ , respectively, and  $N_t$  denotes the number of snapshots. For the wall-bounded flows, the grid sizes correspond to the streamwise ( $x$ ), wall-normal ( $y$ ), and spanwise directions ( $z$ ) and, for the jets, they correspond to the streamwise ( $x$ ), radial ( $r$ ), and azimuthal ( $\theta$ ) directions, respectively.

---

original BL0729 and BL1024 simulations employed second-order accurate staggered finite differences; however, the published datasets are collocated and subsampled by a factor of two in  $y$  and  $z$  (Towne *et al.* 2023). As a result, we employ collocated finite differences with  $N_s = 3$  in  $x$  and  $y$ . Since the  $z$  direction has periodic boundary conditions, we compute spanwise derivatives using a spectral method with the modified wavenumbers associated with the original staggered finite difference scheme. The original Jet0.4 and Jet0.9 simulations employed an unstructured grid (Brès *et al.* 2018) and the corresponding datasets are interpolated onto a structured cylindrical grid. As such, we use collocated finite differences with  $N_s = 3$  in  $x$  and  $r$  and a spectral method in  $\theta$ .

#### 4. Partitioning in nearly-isotropic turbulence

The isotropic velocity gradient partitioning characterizes the contributions of  $\mathbf{A}_\epsilon$ ,  $\mathbf{A}_\varphi$ , and  $\mathbf{A}_\gamma$  in the idealized setting of forced isotropic turbulence. It has been established previously for  $Re_\lambda \approx 1 - 588$  (Das & Girimaji 2020) and is roughly invariant for  $Re_\lambda \gtrsim 200$ . Here, we use FIT610 to confirm this isotropic partitioning, which we denote by  $(\cdot)^{iso}$ . We characterize deviations from this partitioning using the following metric,

$$\Delta^{iso} = \frac{\sum_{\zeta \in \{\epsilon, \varphi, \gamma, \varphi\gamma\}} \left| \langle A_\zeta^2 \rangle_{A^2} - \langle A_\zeta^2 \rangle_{A^2}^{iso} \right|}{\sum_{\zeta \in \{\epsilon, \varphi, \gamma, \varphi\gamma\}} \left| \langle A_\zeta^2 \rangle_{A^2}^{iso} \right|}, \quad (4.1)$$

in which the denominator sums to unity. One advantage of this metric is that it is not affected by further decomposing  $\mathbf{A}_\gamma$  into its symmetric and antisymmetric parts. In the present study, this metric produces results similar to those produced by relative root-mean-square deviations, which are more commonplace.

Table 2 shows the partitioning alongside this metric for each dataset. Consistent with previous results (Das & Girimaji 2020), the FIT315 partitioning is nearly identical to the FIT610 partitioning. For the remaining flows, the partitioning is taken from regions where the mean shearing is relatively weak. Further, for the boundary layers and jets, it is taken sufficiently far from the T/NT interface to mitigate the imprint of the exterior potential flow. For Ch1000, BL0729, and BL1024, the partitioning in these regions is remarkably similar to the isotropic partitioning, with deviations of less than 1%. This is true to a lesser extent for both jets, which have deviations of less than 3%. These results highlight that the isotropic partitioning is broadly applicable in appropriate regions of inhomogeneous turbulent flows.

Case	$\Delta^{iso} (\%)$	$\langle A_\epsilon^2 \rangle_{A^2}$	$\langle A_\varphi^2 \rangle_{A^2}$	$\langle A_\gamma^2 \rangle_{A^2}$	$\langle A_{\varphi\gamma}^2 \rangle_{A^2}$
FIT315	0.2	0.239	0.106	0.521	0.134
FIT610	–	0.240	0.106	0.520	0.134
Ch0186	5.0	0.250	0.090	0.535	0.125
Ch1000	0.4	0.242	0.105	0.519	0.134
BL0729	0.8	0.244	0.103	0.519	0.134
BL1024	0.4	0.240	0.104	0.520	0.136
Jet0.4	2.6	0.251	0.107	0.507	0.135
Jet0.9	2.2	0.250	0.105	0.510	0.135

Table 2: Velocity gradient partitioning for each flow and the corresponding deviation metrics. The partitioning is reported at the channel centerline for Ch0186 and Ch1000 and at  $(Re_\tau, y^+) \approx (729, 149)$  and  $(1000, 144)$  for BL0729 and BL1024, respectively. For both Jet0.4 and Jet0.9, it is reported at  $(x/D, r/D) \approx (20, 1)$ , where  $D$  is the nozzle diameter. The column shadings reflect our partitioning color scheme.

## 5. Partitioning in wall-bounded turbulence

### 5.1. Effect of mean shearing

For wall-bounded turbulent flows, the velocity gradient partitioning is heavily influenced by the mean shearing imposed by the wall. [Figure 1](#) shows the partitioning profiles as a function of wall-normal location in inner units and as a function of mean shearing strength. Consistent with [table 2](#), the partitioning approaches the isotropic values far from the wall, starting from the top of the log-law region. However, the boundary layer partitioning begins to diverge from these values near the edge of the boundary layer, reflecting the transition to a potential flow. Beyond the boundary layer thickness (not shown), this transition is associated with monotonic enhancement of axial straining and decay of the other constituents. Consistent with the results in [table 2](#), the Ch0186 partitioning does not converge as well onto the isotropic values since it is barely turbulent. The partitioning throughout this minimal channel is generally associated with enhanced contributions from shearing.

For the wall-normal profiles in [figure 1](#), the near-wall partitioning is dominated by shearing. This feature reflects the strong imprint of the mean shearing on the near-wall velocity gradient fluctuations. Between the near-wall regime and the nearly-isotropic regime far from the wall, there is particularly striking collapse of the partitioning profiles for BL0729, BL1024, and (to a lesser extent) Ch1000. The most significant differences between the channel and boundary layer profiles occur in the buffer layer. For the channels, the contributions of shearing and axial straining in this region are enhanced and reduced, respectively, relative to their contributions in the boundary layers. While beyond the scope of the present work, characterizing how the turbulence structures in the buffer layer reflect these differences would be interesting future work.

The mean shearing strength profiles in [figure 1](#) provide a complementary view to the wall-normal profiles. The mean shearing strength parameter is normalized as  $\bar{A}_\gamma^2 / \bar{A}_{\gamma,w}^2$ , where  $\bar{A}_{\gamma,w}^2$  represents the (maximum) value at the wall. This parameter quantifies the effect of the wall in terms of velocity gradients and can be determined directly from the mean flow. Further, for the channels and boundary layers we consider, it can be well-approximated using a single mean flow gradient,  $\partial \bar{u} / \partial y$ . For these profiles, we primarily focus on the buffer layer and log-law region since they capture the majority of the evolution from the near-wall regime to the nearly-isotropic regime. As observed in the wall-normal profiles, the partitioning in these regions collapses very well as a function of the mean shearing strength for BL0729, BL1024, and (to a lesser extent) Ch1000.

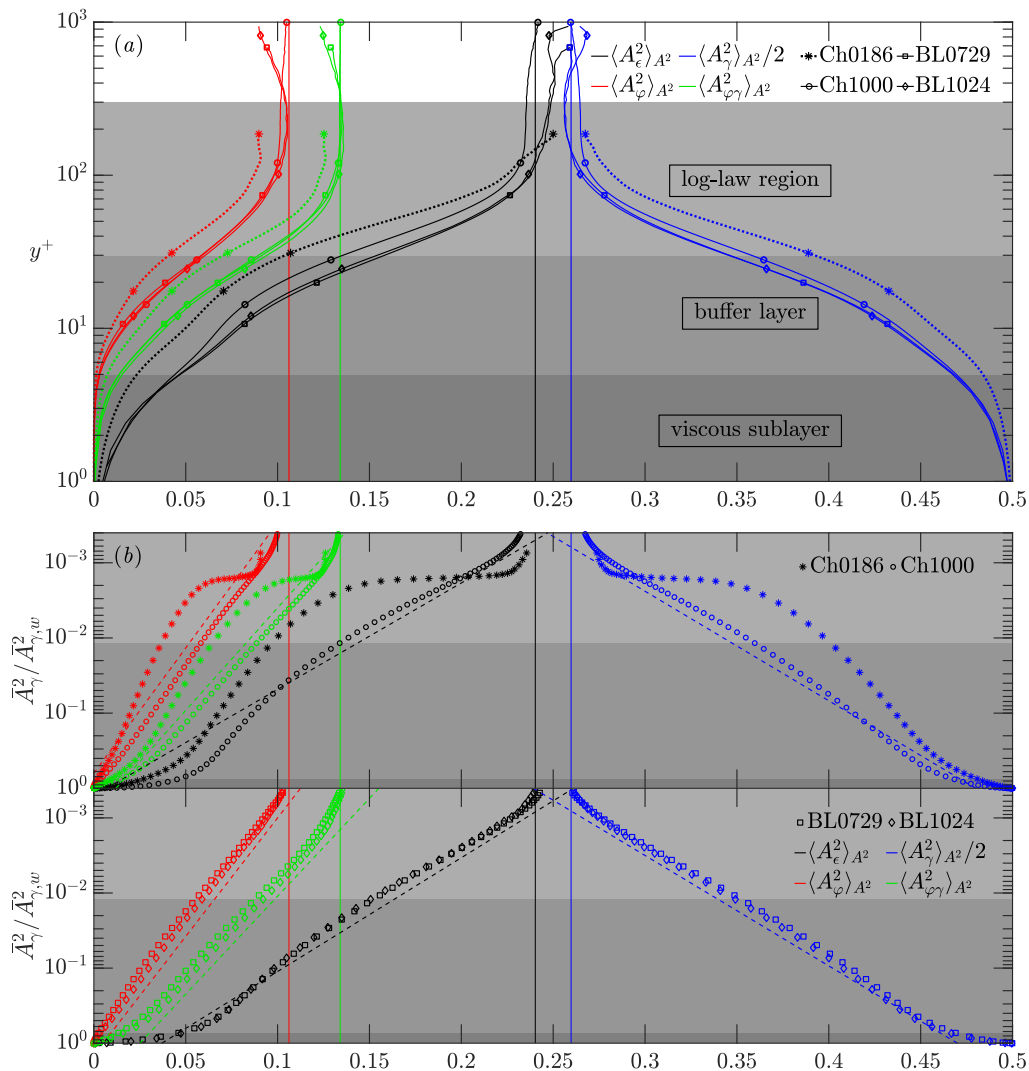


Figure 1: Velocity gradient partitioning profiles for the channels and boundary layers in terms of wall-normal location in inner units (a) and mean shearing strength (b). The vertical lines represent the isotropic values. The BL0729 and BL1024 profiles are shown for  $Re_\tau \approx 729$  and 1000, respectively, and the top boundary of the log-law region represents Ch1000. In (a), the markers are used to distinguish between the profiles and, in (b), they represent actual data points. The mean shearing axis in (b) is reversed to match the style of (a) and the dashed lines represent comparable linear-log trends, with the partitioning as the dependent variable.

One interesting feature of the collapsed profiles in these regions is that they appear to vary nearly linearly with  $\log(\bar{A}_\gamma^2 / \bar{A}_{\gamma,w}^2)$ , especially for the contributions of rigid rotation and shear-rotation interactions. The dashed lines in figure 1 empirically characterize the slopes of these linear-log variations for each partitioning constituent. The empirical slopes for  $(\langle A_\epsilon^2 \rangle_{A^2}, \langle A_\varphi^2 \rangle_{A^2}, \langle A_\gamma^2 \rangle_{A^2} / 2, \langle A_{\varphi\gamma}^2 \rangle_{A^2})$  are approximately  $(-0.029, -0.014, 0.030, -0.017)$  for BL0729 and BL1024 and  $(-0.031, -0.013, 0.030, -0.016)$  for Ch1000. The variations in axial straining and pure shearing do not follow these scalings as closely as the variations in rigid rotation and shear-rotation interactions.



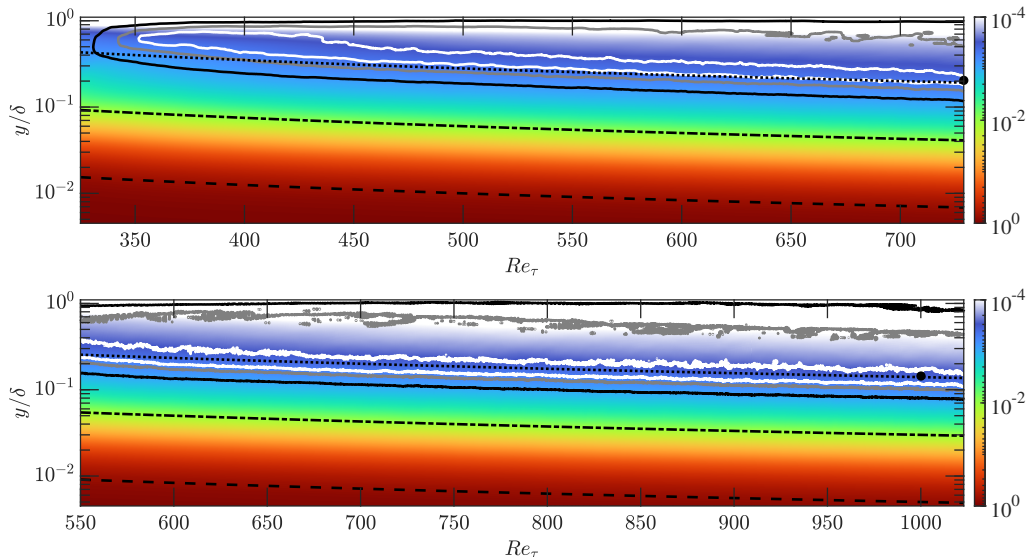


Figure 2: Streamwise development of BL0729 (top) and BL1024 (bottom) in terms of  $Re_\tau$ . The color axis represents  $\bar{A}_y^2 / \bar{A}_{y,w}^2$  and the contours represent  $\Delta^{iso} = 1\%$  (white),  $\Delta^{iso} = 2\%$  (gray), and  $\Delta^{iso} = 5\%$  (black). The dashed, dash-dotted, and dotted black lines represent the top of the viscous sublayer ( $y^+ = 5$ ), the top of the buffer layer ( $y^+ = 30$ ), and  $y^+ = 140$ , respectively. The black circles represent the locations of partitioning values reported in [table 2](#) and  $\delta$  represents the boundary layer thickness.

For the isotropic partitioning, it is known that  $\langle A_\epsilon^2 \rangle_{A^2} \sim \langle A_\varphi^2 \rangle_{A^2} + \langle A_{\varphi\gamma}^2 \rangle_{A^2} \sim \langle A_y^2 \rangle_{A^2} / 2$  (Das & Girimaji 2020). For wall-bounded flows, we show that these similarities also apply to the magnitudes of the slopes used to characterize the linear-log variations as a function of the mean shearing strength. More rigorously modeling these variations would help enable predictions of the partitioning profiles in terms of mean flow variables. While we do not propose an explicit model for these variations in the present study, our analysis suggests that the mean shearing is appropriate for modeling the velocity gradient partitioning and sufficiently high  $Re_\tau$ .

## 5.2. Effect of friction Reynolds number

Beyond wall-normal variations, the streamwise spatial development in the boundary layers is associated with increasing  $Re_\tau$ . [Figure 2](#) shows how the region where the isotropic partitioning is applicable evolves as a function of  $Re_\tau$ . For BL0729, this region grows appreciably in size as  $Re_\tau$  increases. The same is true to a lesser extent for BL1024, where the turbulence is more well-developed throughout the domain. The  $\Delta^{iso} = 1\%$  contours identify the region where the isotropic partitioning is most applicable. This region is concentrated near  $y^+ \approx 140$ , which scales in inner units, throughout BL1024 and at the downstream end of BL0729. This contrasts with the boundary layer thickness, which scales in outer units and captures the divergence from the isotropic partitioning near the freestream. These results suggest that inner unit scalings can be used to determine when the partitioning approaches the isotropic values, but that outer unit scalings must be used to capture the divergence to a potential flow in the boundary layers. They further suggest that  $Re_\tau \gtrsim 700$  is a reasonable regime in which to expect a collapsed partitioning. This estimate is consistent with the collapse of the partitioning profiles for BL0729, BL1024 and (to a lesser extent) Ch1000 as well as the lack of collapse for Ch0186 in [figure 1](#).

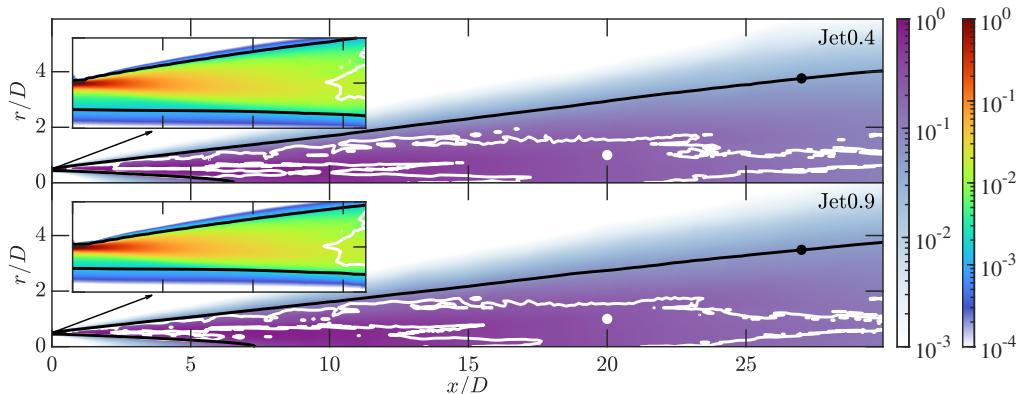


Figure 3: Spatial development of Jet0.4 and Jet0.9. For the larger plots, the color axis represents the turbulent kinetic energy normalized by its maximum value. The inset plots magnify the region near the nozzle lip,  $(x/D, r/D) \in [0, 0.65] \times [0.4, 0.6]$ , and their color axis represents the mean shearing strength normalized by its maximum value (at the nozzle lip). The white contours represent  $\Delta^{iso} = 5\%$  and the black contours identify the interior and exterior edges of the jet as where the mean streamwise velocity is 95% and 5% of the jet velocity, respectively. The white and black circles represent the locations of the partitioning values reported in table 2 and table 3, respectively.

Case	$\Delta^{iso} (\%)$	$\langle A_\epsilon^2 \rangle_{A^2}$	$\langle A_\varphi^2 \rangle_{A^2}$	$\langle A_\gamma^2 \rangle_{A^2}$	$\langle A_{\varphi\gamma}^2 \rangle_{A^2}$
Arun & Colonius (2024)	14.8	0.280	0.133	0.446	0.141
Jet0.4	13.4	0.285	0.124	0.453	0.138
Jet0.9	13.4	0.290	0.121	0.453	0.136

Table 3: Partitioning near the T/NT interface in the jets, taken from  $(x/D, r/D) \approx (26.9, 3.76)$  for Jet0.4 and  $(x/D, r/D) \approx (26.9, 3.53)$  for Jet0.9. The partitioning for a decaying turbulent cloud produced by a vortex ring collision (Arun & Colonius 2024) is also shown for reference.

## 6. Partitioning in jet turbulence

In the jets we consider, the mean flow shear layer decays rapidly near the nozzle lip. As depicted in figure 3, this implies that the isotropic partitioning is broadly applicable within the turbulent interior of the jets. Specifically, the isotropic partitioning becomes applicable when the mean shearing strength decreases two orders of magnitude from its maximum value (at the nozzle lip). By contrast, for the wall bounded flows (see §5), it becomes applicable when the mean shearing strength decreases three orders of magnitude from its maximum value (at the wall). We do not further characterize the partitioning as a function of the mean shearing for the jets since the data interpolated from the large-eddy simulations have limited resolution in the region near the nozzle lip. A more detailed analysis of this region, especially using direct numerical simulations, would entail useful future work.

We instead focus on the downstream partitioning, where the jet turbulence is well-developed. Specifically, we identify how the partitioning well within the turbulent jet differs from the partitioning near the T/NT interface, where the turbulent kinetic energy is significantly lower. The latter region separates the fully turbulent interior of the jet from the exterior, which is well-approximated as a potential flow and primarily associated with axial straining.



Similar to the boundary layers, the partitioning far from the T/NT interface in the jets is close to the isotropic partitioning. For the boundary layers, the transition to the potential flow regime is associated with the decay of all contributions except axial straining (see §5). The partitioning near the T/NT interface in the jets is also associated with enhanced axial straining and reduced shearing. However, before diverging to the potential flow regime, it is associated with an enhanced contribution of rigid rotation relative to the isotropic partitioning.

Table 1 exemplifies this enhanced contribution of rigid rotation using points taken from the 5% contour of the mean streamwise velocity. The partitioning at these points is actually more similar to that of a decaying turbulent cloud (Arun & Colonius 2024) than it is to the isotropic partitioning. However, we emphasize that the turbulence in the jets does not decay in time since the turbulent kinetic energy is stationary. As such, characterizing why the contribution from rigid rotation increases (instead of decaying monotonically) in this region, e.g., by visualizing the flow structures in this region, would be interesting future work. Addressing whether this feature reflects the geometry of the jets or the nature of their spatial development would be particularly useful.

## 7. Concluding remarks

We have analyzed the partitioning of velocity gradient fluctuations based on the triple decomposition in several canonical turbulent flows. The partitioning we compute for forced isotropic turbulence agrees well with previous results (Das & Girimaji 2020).

Moreover, we show that the isotropic partitioning also applies to velocity fluctuations near and beyond the top of the log-law region in wall-bounded flows over a broad range of  $Re_\tau$ . For the boundary layers we consider, it becomes most applicable around  $y^+ \approx 140$  for  $Re_\tau \gtrsim 700$ . The partitioning profiles collapse well at sufficiently high  $Re_\tau$  as they transition from the shearing-dominated near-wall regime to the nearly-isotropic regime. Further, the mean shearing provides a reasonable mean flow parameter for modeling their variations in the buffer layer and the log-law region.

We also show that the isotropic partitioning is broadly applicable to subsonic and transonic jets in regimes of practical relevance. This broad applicability is attributed to the rapid decay of the mean flow shear layer near the nozzle lip. Before reaching the exterior potential flow regime, the partitioning near the T/NT interface in the jets is associated with an enhanced contribution of rigid rotation relative to the isotropic partitioning.

Moving forward, analyzing the partitioning profiles at higher  $Re_\tau$  would help further characterize their sensitivity and collapse for wall-bounded flows. Developing more rigorous models for the partitioning in terms of mean flow variables would also be useful, especially models that do not depend strongly on the flow configuration. Finally, connecting the statistical features we report to the turbulence structures that produce them would provide an enhanced view of the roles of the partitioning constituents.

**Acknowledgements.** The authors gratefully acknowledge A. Nekkanti and M. Wadas for helpful discussions and H. J. Bae for providing the Ch0186 dataset.

**Funding.** R.A. was supported by the Department of Defense (DoD) through the National Defense Science & Engineering Graduate (NDSEG) Fellowship Program.

**Declaration of interests.** The authors report no conflict of interest.

### Author ORCIDs.

① Rahul Arun <https://orcid.org/0000-0002-5942-169X>

② Tim Colonius <https://orcid.org/0000-0003-0326-3909>

## REFERENCES

- ARUN, R., BAE, H. J. & McKEON, B. J. 2023 Towards real-time reconstruction of velocity fluctuations in turbulent channel flow. *Phys. Rev. Fluids* **8** (6), 064612.
- ARUN, R. & COLONIUS, T. 2024 Velocity gradient analysis of a head-on vortex ring collision. *J. Fluid Mech.* **982**, A16.
- BEAUMARD, P., BUXTON, O. R. H. & KEYLOCK, C. J. 2019 The importance of non-normal contributions to velocity gradient tensor dynamics for spatially developing, inhomogeneous, turbulent flows. *J. Turbul.* **20** (9), 577–598.
- BRÈS, G. A., JORDAN, P., JAUNET, V., LE RALLIC, M., CAVALIERI, A. V. G., TOWNE, A., LELE, S. K., COLONIUS, T. & SCHMIDT, O. T. 2018 Importance of the nozzle-exit boundary-layer state in subsonic turbulent jets. *J. Fluid Mech.* **851**, 83–124.
- CARDESA, J. I., VELA-MARTÍN, A. & JIMÉNEZ, J. 2017 The turbulent cascade in five dimensions. *Science* **357** (6353), 782–784.
- DAS, R. & GIRIMAJI, S. S. 2020 Revisiting turbulence small-scale behavior using velocity gradient triple decomposition. *New J. Phys.* **22** (6), 063015.
- ENOKI, R., WATANABE, T. & NAGATA, K. 2023 Statistical properties of shear and nonshear velocity components in isotropic turbulence and turbulent jets. *Phys. Rev. Fluids* **8** (10), 104602.
- GAO, Y. & LIU, C. 2018 Rortex and comparison with eigenvalue-based vortex identification criteria. *Phys. Fluids* **30** (8), 085107.
- GAO, Y. & LIU, C. 2019 Rortex based velocity gradient tensor decomposition. *Phys. Fluids* **31** (1), 011704.
- GRAHAM, J., KANOV, K., YANG, X. I. A., LEE, M., MALAYA, N., LALESCU, C. C., BURNS, R., EYINK, G., SZALAY, A., D., MOSER, R. & MENEVEAU, C. 2016 A Web services accessible database of turbulent channel flow and its use for testing a new integral wall model for LES. *J. Turbul.* **17** (2), 181–215.
- HEIDT, L., COLONIUS, T., NEKKANTI, A., SCHMIDT, O. T., MAIA, I. & JORDAN, P. 2023 Cyclostationary analysis of forced turbulent jets. In *AIAA Aviation 2023 Forum*, p. 3652.
- JIMÉNEZ, J. & MOIN, P. 1991 The minimal flow unit in near-wall turbulence. *J. Fluid Mech.* **225**, 213–240.
- JOHNSON, P. L. & WILCZEK, M. 2024 Multiscale velocity gradients in turbulence. *Annu. Rev. Fluid Mech.* **56**, 463–490.
- KEYLOCK, C. J. 2018 The Schur decomposition of the velocity gradient tensor for turbulent flows. *J. Fluid Mech.* **848**, 876–905.
- KOLÁŘ, V. 2004 2D velocity-field analysis using triple decomposition of motion. In *Proceedings of the 15th Australasian Fluid Mechanics Conference*, p. AFMC00017. The University of Sydney.
- KOLÁŘ, V. 2007 Vortex identification: new requirements and limitations. *Int. J. Heat Fluid Flow* **28** (4), 638–652.
- KRONBORG, J. & HOFFMAN, J. 2023 The triple decomposition of the velocity gradient tensor as a standardized real Schur form. *Phys. Fluids* **35** (3), 031703.
- LI, Y., PERLMAN, E., WAN, M., YANG, Y., MENEVEAU, C., BURNS, R., CHEN, S., SZALAY, A. & EYINK, G. 2008 A public turbulence database cluster and applications to study Lagrangian evolution of velocity increments in turbulence. *J. Turbul.* **9**, N31.
- LIU, C., GAO, Y., TIAN, S. & DONG, X. 2018 Rortex—a new vortex vector definition and vorticity tensor and vector decompositions. *Phys. Fluids* **30** (3), 035103.
- MENEVEAU, C. 2011 Lagrangian dynamics and models of the velocity gradient tensor in turbulent flows. *Annu. Rev. Fluid Mech.* **43**, 219–245.
- TOWNE, A., DAWSON, S. T. M., BRÈS, G. A., LOZANO-DURÁN, A., SAXTON-FOX, T., PARTHASARATHY, A., JONES, A. R., BILER, H., YEH, C.-A., PATEL, H. D. & TAIRA, K. 2023 A database for reduced-complexity modeling of fluid flows. *AIAA J.* **61** (7), 2867–2892.
- WU, Y., ZHANG, W., WANG, Y., ZOU, Z. & CHEN, J. 2020 Energy dissipation analysis based on velocity gradient tensor decomposition. *Phys. Fluids* **32** (3), 035114.
- YEUNG, P. K., DONZIS, D. A. & SREENIVASAN, K. R. 2012 Dissipation, enstrophy and pressure statistics in turbulence simulations at high Reynolds numbers. *J. Fluid Mech.* **700**, 5–15.